

Engineering Subwavelength Nanoantennas in the Visible by Employing Resonant Anisotropic Nanospheroids

Georgios D. Kolezas¹, *Student Member, IEEE*, Grigorios P. Zouros², *Senior Member, IEEE*, and Kosmas L. Tsakmakidis

Abstract—We analyze the engineering of subwavelength nanoantennas composed of anisotropic nanospheroids, for the development of photonic devices. Instead of using conventional isotropic dielectrics, we introduce resonant anisotropic nanoparticles, allowing for shifting Kerker condition points further inside the visible. To address this study, we construct a perturbation-based discrete eigenfunction method, for the electromagnetic scattering of a plane wave by a prolate or oblate uniaxial anisotropic spheroid. The method is fast and yields the solution for the bistatic radar and total scattering cross sections, which is valid for small eccentricities of the spheroid. The validity of this technique is verified by the alternative general purpose discrete dipole approximation method. We investigate the engineering of subwavelength nanoantennas due to material and geometry shaping, like the change of anisotropy type, anisotropy ratio, and deviation of the nanoantenna from sphericity.

Index Terms—Anisotropic, dispersive, nanoantenna, nanophotonics, perturbation, spheroid, subwavelength, uniaxial.

I. INTRODUCTION

LATELY, there is a growing interest in exploiting the scattering characteristics of resonant subwavelength photonic nanostructures for the development of integrated optical devices, like two-dimensional plasmonic arrays composed of patches and rings for electric field enhancement [1], nanocylindrical arrays for the degeneration of guided waves [2], or meta-optics devices for manipulating optical waves [3]. Of particular interest are dielectric subwavelength spheres, whose directional scattering characteristics are employed in nanoantenna design. The main platform material is Si due to its high refractive index [4], [5], although Ge [6] and Cu₂O [7] are also used. These high-index dielectrics exhibit both electric and magnetic resonances [8], and offer greater design flexibility in the nanoscale,

Manuscript received August 1, 2018; revised December 21, 2018; accepted February 20, 2019. Date of publication March 8, 2019; date of current version April 12, 2019. The work of G. P. Zouros and K. L. Tsakmakidis was supported by the Hellenic Foundation for Research and Innovation (HFRI) and by the General Secretariat for Research and Technology (GSRT) under Grant 1819. (*Corresponding author: Grigorios P. Zouros*).

G. D. Kolezas and G. P. Zouros are with the School of Electrical and Computer Engineering, National Technical University of Athens, Athens 15773, Greece (e-mail: geokolezas@central.ntua.gr; zouros@ieee.org).

K. L. Tsakmakidis is with the Department of Physics, National and Kapodistrian University of Athens, Athens 15784, Greece (e-mail: ktsakmakidis@phys.uoa.gr).

Color versions of one or more of the figures in this paper are available online at <http://ieeexplore.ieee.org>.

Digital Object Identifier 10.1109/JSTQE.2019.2902906

in contrast to plasmonic-based particles [9]–[11], which are characterized by intrinsic losses in the visible range. In particular, high-index dielectrics have been utilized for the composition of nanoantennas through highly transparent Huygens metasurfaces, or optical sensors and nonlinear devices [12]. High-index silicon nanodisks embedded into low-index matrix have been used to manipulate the directional scattering properties of the nanoantenna [13], and individual spherical silicon nanoparticles have allowed for tailoring the chirality of light [14]. Collective near field interactions have been employed in the design of directional beams by utilizing near field power flow [15], and in the design of metamaterials using superlattice structures based on split ring resonators [16], or combined dielectric-metallic structures composed of spherical-split ring resonators [17].

The majority of aforementioned works focus on spherical nanostructures. In some circumstances, however, scanning electron microscopy (SEM) images reveal that the fabricated nanoparticles exhibit slight deviations from the spherical shape [5]. To account for the modification of scattering characteristics due to these small deviations from sphericity, full wave finite-difference time-domain (FDTD) simulations [5], and solution of the wave equation in spheroidal coordinates [18], have been proposed, where now the particle is modeled as a spheroid. However, the application of numerical full wave techniques requires extremely fine discretization and high CPU time to obtain a meaningful result, whereas spheroidal wavefunctions are characterized by cumbersome convergence and require careful truncation of resulting infinite sets of equations [19], [20]. In addition, these methods cannot distinguish accurately and fast the response of such small deviations in shape, as an exact analytical technique does. Moreover, the above works deal with isotropic particles, a case which can also be tackled by well known techniques [20]–[22]. On the contrary, the introduction of anisotropy and the study of its effect on the properties of resonant nanostructures are topics open to investigation.

These facts motivate us to extend the study of EM scattering by subwavelength isotropic nanospheres/nanospheroids to anisotropic ones. In order to account for spheroidal shapes, we apply a perturbation method capable of detecting small deviations from sphericity. It is shown that these deviations lead to significant shifts in magnetic/electric dipolar (MD)/(ED) resonances, and in sequence in Kerker wavelengths, thus enabling to tune the wavelength of the forward directional radiation, by

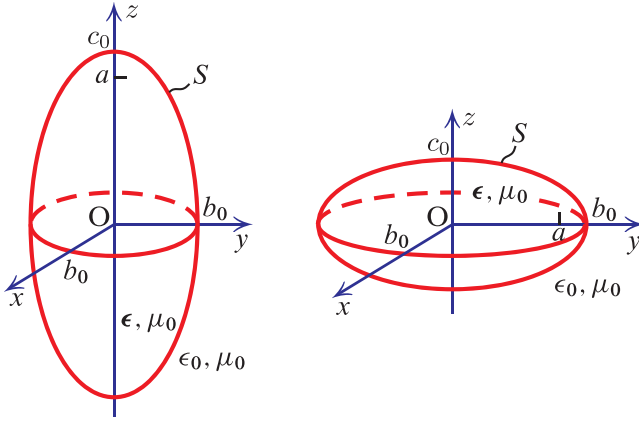


Fig. 1. Geometry of the spheroidal scatterer. Left: prolate; right: oblate.

tailoring the shape of the nanoparticle. Non sphericity is combined with anisotropy by introducing the concept of resonant anisotropic nanoparticles where, instead of isotropic dielectrics, uniaxial anisotropic materials are used to form the nanoantenna. The use of dispersive uniaxial semiconductor crystals, such as TiO_2 and ZnGeP_2 , ensures the unidirectional properties of the nanoantenna as isotropic ones do, since they exhibit high ordinary/extraordinary refractive indices throughout the visible range [23]. Moreover, the main advantage of using uniaxial anisotropic materials, is that the high difference in ordinary/extraordinary indices, enables to push the overlapping MD/ED point—first Kerker condition point—further inside the visible, towards blue.

Existing methods that deal with light scattering by anisotropic non spherical particles, include a Galerkin based integral equation technique for the case of an anisotropic ellipsoid [24], and the T-matrix method for rotationally uniaxial particles [25] and uniaxial ellipsoids [26]. However, as these remain numerical methods, in this work we construct a fast and accurate asymptotic solution to the scattering of a plane EM wave by an anisotropic prolate or oblate spheroid, valid for small deviations from sphericity. The geometry of the scatterer is shown in Fig. 1. The prolate/oblate spheroid has a semi-major axis of length c_0/b_0 , a semi-minor axis of length b_0/c_0 , an interfocal distance $2a$, an eccentricity $h = a/c_0$, and a boundary surface S . For the prolate spheroid $0 \leq h \leq 1$, and for the oblate spheroid $0 \leq h < \infty$ [27]. When $h = 0$, both prolate/oblate spheroids degenerate to a sphere of radius $R = c_0 \equiv b_0$, the case $h = 1$ turns the prolate spheroid to a needle having height $2a$, and the case $h \rightarrow \infty$ turns the oblate spheroid to a disk of radius a . The spheroid has uniaxial properties in permittivity, while its permeability is equal to that of free space. The uniaxial anisotropy is described by Cartesian permittivity tensor

$$\epsilon = \begin{bmatrix} \epsilon_o & 0 & 0 \\ 0 & \epsilon_o & 0 \\ 0 & 0 & \epsilon_e \end{bmatrix}. \quad (1)$$

In (1), $\epsilon_o = \epsilon_{or}\epsilon_0$ and $\epsilon_e = \epsilon_{er}\epsilon_0$ correspond to ordinary and extraordinary tensorial elements, respectively, where ϵ_{or} and

ϵ_{er} are the relative permittivity elements. The respective refractive indices are $n_o = \sqrt{\epsilon_{or}}$ and $n_e = \sqrt{\epsilon_{er}}$. The surrounding medium is considered to be free space with ϵ_0/μ_0 as the free space permittivity/permeability.

In order to solve the problem at hand, we initially expand the incident and scattered fields in the surrounding region, as well as the transmitted field in the anisotropic region, in terms of spherical vector wave functions (SVWFs). For the field expansion in the region of anisotropy, we make use of the method originally developed for gyromagnetic spheres in [28]—hereinafter referred to as DEM. DEM is based on the expansion of the unknown fields in the anisotropic region in terms of SVWFs with discrete wavenumbers, the latter obtained from the solution of an eigenvalue problem. As long as h is kept small, the spheroid is treated as a perturbation of the respective sphere with $R = c_0$. Thus, we apply Maclaurin series expansion versus h for the incident, scattered and transmitted fields, and in sequence for the boundary conditions (BCs), at the perturbed spherical boundary. This results—after great analytical effort—in simple algebraic expressions for the bistatic and total scattering cross sections, valid for small values of h . The main advantage of this method is that it provides fast and accurate results in the appropriate range of small values of h , while numerical techniques require many repetitions and high CPU time for convergence. The validity of our method is verified by comparisons with a particular version of DDA, i.e., ADDA code [29], which supports uniaxial anisotropy.

It should be noted that this perturbation procedure was applied in [19], [20] to construct a closed-form solution for metallic and isotropic spheroids. This work has the following novelty points as compared to [19], [20]: first, the present method requires the numerical solution of an eigenvalue problem involving the elements of the anisotropic permittivity tensor. This means that the closed-form expressions of [20] cannot be used in the present case, and a different approach is followed to solve the perturbed problem. This approach is based on the successive solution of linear systems of different orders (see Section II). Second, it extends the study of EM scattering by metallic/isotropic to anisotropic spheroids. This extension is not trivial, since the use of the formal series solution based on spheroidal wavefunctions [20, Section III] cannot be applied in anisotropic domains.

Once the method is developed, it is applied in investigating how the engineering of subwavelength nanoantennas can be achieved, due to the change of various parameters, like (i) the anisotropy type (positive/negative uniaxial), (ii) anisotropy ratio ($\text{AR} \equiv |(\epsilon_o - \epsilon_e)/(\epsilon_o + \epsilon_e)|$), (iii) the deviation from sphericity through eccentricity h , (iv) the angle of incidence, and (v) the type of incidence (transverse electric (TE) and transverse magnetic (TM)).

This paper is organized as follows: Section II presents the solution to the scattering problem. Section III examines the validity and efficiency of the proposed method, Section IV investigates anisotropic nanospheroids at subwavelength scale, Section V concludes, and Appendix includes various analytical expressions needed for the application of the method.

II. EM SCATTERING BY ANISOTROPIC SPHEROIDS

A. Prolate Spheroid

We consider a prolate spheroid illuminated by a plane EM wave. The incident electric field has the expansion [28]

$$\mathbf{E}^{\text{inc}} = -i \sum_{\substack{m=-\infty \\ n=|m|}}^{\infty} \bar{E}_{mn} \left[q_{mn} \mathbf{M}_{mn}^{(1)}(k_0, \mathbf{r}) + p_{mn} \mathbf{N}_{mn}^{(1)}(k_0, \mathbf{r}) \right], \quad (2)$$

with k_0 the free space wavenumber, while the expansion coefficients q_{mn} , p_{mn} are derived from expressions given in [28], depending on the wave's polarization and direction of propagation. The stacked notation in the subscript of summation sign denotes double summation from $m = -\infty/n = |m|$ to $m = \infty/n = \infty$. The $e^{-i\omega t}$ time dependence is assumed and suppressed throughout.

The transmitted electric field inside the spheroid has the form [30]

$$\begin{aligned} \mathbf{E}^{\text{t}} = & -i \sum_{\substack{m=-\infty \\ n=|m|}}^{\infty} \bar{E}_{mn} \sum_{l=1}^{\infty} a_l \left[c_{mnl} \mathbf{M}_{mn}^{(1)}(k_l, \mathbf{r}) \right. \\ & + d_{mnl} \mathbf{N}_{mn}^{(1)}(k_l, \mathbf{r}) + \frac{\bar{w}_{mnl}}{\lambda_l} \mathbf{L}_{mn}^{(1)}(k_l, \mathbf{r}) \\ & \left. - i \sum_{l=1}^{\infty} \frac{a_l w_{00l}}{\lambda_l} \mathbf{L}_{00}^{(1)}(k_l, \mathbf{r}), \right] \end{aligned} \quad (3)$$

while the scattered field is expressed as

$$\mathbf{E}^{\text{s}} = -i \sum_{\substack{m=-\infty \\ n=|m|}}^{\infty} \bar{E}_{mn} \left[a_{mn} \mathbf{M}_{mn}^{(3)}(k_0, \mathbf{r}) + b_{mn} \mathbf{N}_{mn}^{(3)}(k_0, \mathbf{r}) \right]. \quad (4)$$

In above field expansions, $\bar{E}_{mn} = i^n [(2n+1)(n-m)!/n/(n+1)/(n+m)!]^{1/2}$, and $\mathbf{M}_{mn}^{(j)}$, $\mathbf{N}_{mn}^{(j)}$, $\mathbf{L}_{mn}^{(j)}$, $j = 1, 3$, are the SVWFs, given by [31]

$$\begin{aligned} \mathbf{M}_{mn}^{(j)}(k, \mathbf{r}) &= \sqrt{n(n+1)} z_n^{(j)}(kr) \mathbf{C}_{mn}(\theta, \varphi), \\ \mathbf{N}_{mn}^{(j)}(k, \mathbf{r}) &= n(n+1) \frac{z_n^{(j)}(kr)}{kr} \mathbf{P}_{mn}(\theta, \varphi) \\ &+ \sqrt{n(n+1)} \frac{1}{kr} \frac{d[rz_n^{(j)}(kr)]}{dr} \mathbf{B}_{mn}(\theta, \varphi), \\ \mathbf{L}_{mn}^{(j)}(k, \mathbf{r}) &= \frac{1}{k} \frac{dz_n^{(j)}(kr)}{dr} \mathbf{P}_{mn}(\theta, \varphi) \\ &+ \sqrt{n(n+1)} \frac{z_n^{(j)}(kr)}{kr} \mathbf{B}_{mn}(\theta, \varphi), \end{aligned} \quad (5)$$

where $z_n^{(1)} = j_n$ is the spherical Bessel function, $z_n^{(3)} = h_n$ is the spherical Hankel function of the first kind with superscript (1) omitted for simplicity, and \mathbf{P}_{mn} , \mathbf{B}_{mn} , \mathbf{C}_{mn} are the spherical surface harmonic vectors (SSHVs) [32]. We point out that in the sums over m and n in expansions (2)–(4), the pair $(m, n) = (0, 0)$ is excluded. The expressions of coefficients

\bar{w}_{mnl} , w_{00l} can be found in [30]. Furthermore, the quantities c_{mnl} , d_{mnl} , λ_l are obtained by solving an eigenvalue problem as described in detail in [30]. The coefficient matrix of the eigenvalue problem depends on the tensorial permittivity elements. Finally, the discrete wavenumber k_l is given by $k_l = \tau_l k_0$, with $\tau_l = \sqrt{\epsilon_{er}/\lambda_l}$. The respective magnetic fields \mathbf{H}^{inc} , \mathbf{H}^{t} , \mathbf{H}^{s} , can be found by Faraday's law $\mathbf{H} = -i/(\omega\mu_0)\nabla \times \mathbf{E}$.

The solution of the scattering problem requires the satisfaction of the BCs for the electric and the magnetic field at the spheroid's surface S , i.e.,

$$\mathbf{n} \times (\mathbf{E}^{\text{inc}} + \mathbf{E}^{\text{s}} - \mathbf{E}^{\text{t}})|_S = 0, \quad \mathbf{n} \times (\mathbf{H}^{\text{inc}} + \mathbf{H}^{\text{s}} - \mathbf{H}^{\text{t}})|_S = 0, \quad (6)$$

with \mathbf{n} the outwards unit normal vector on S . To this end, we consider small values of the eccentricity h , and treat the spheroid as a perturbed sphere of radius $R = c_0$. As a first step, the surface of the spheroid is expressed in terms of spherical coordinates as $r = c_0/\sqrt{1 - h^2 \sin^2 \theta/(h^2 - 1)}$, $\theta \in [0, \pi]$, and then we take its Maclaurin series expansion in terms of h , yielding

$$r = c_0 \left[1 - \frac{\sin^2 \theta}{2} h^2 - \left(\frac{\sin^2 \theta}{2} - \frac{3 \sin^4 \theta}{8} \right) h^4 + O(h^6) \right]. \quad (7)$$

When (7) is substituted into the radial quantities in SVWFs (5), it gives the asymptotic expansions of the latter at the surface of the spheroid [33, eqs (12) and (13)]. Next, we employ Maclaurin series expansion for \mathbf{n} , i.e.,

$$\begin{aligned} \mathbf{n} = & \left[1 - \frac{h^4 \sin^2(2\theta)}{8} \right] \left[\mathbf{e}_r + \frac{\sin(2\theta)}{2} \right. \\ & \left. \times (h^2 + h^4 \cos^2 \theta) \mathbf{e}_\theta + O(h^6) \right]. \end{aligned} \quad (8)$$

As a further step, for small values of h , the unknown expansion coefficients a_l , a_{mn} , b_{mn} can be expanded as

$$\begin{aligned} a_l &= a_l^{(0)} + a_l^{(2)} h^2 + a_l^{(4)} h^4 + O(h^6), \\ a_{mn} &= a_{mn}^{(0)} + a_{mn}^{(2)} h^2 + a_{mn}^{(4)} h^4 + O(h^6), \\ b_{mn} &= b_{mn}^{(0)} + b_{mn}^{(2)} h^2 + b_{mn}^{(4)} h^4 + O(h^6), \end{aligned} \quad (9)$$

where $a_l^{(0)}$, $a_{mn}^{(0)}$, $b_{mn}^{(0)}$ correspond to the solution of scattering by the unperturbed anisotropic sphere [30]. In order to satisfy the BCs at the spheroid's surface, we substitute into (6) the electric and magnetic field expansions, along with asymptotic expansions (7)–(9). Doing so, and sorting out terms by powers of h , the two BCs transform into two vector equations having the general form

$$\begin{aligned} \mathbf{X}_{mn}^{(0)} + \mathbf{X}_{mn}^{(2)} h^2 + \mathbf{X}_{mn}^{(4)} h^4 + O(h^6) &= 0, \\ \mathbf{Y}_{mn}^{(0)} + \mathbf{Y}_{mn}^{(2)} h^2 + \mathbf{Y}_{mn}^{(4)} h^4 + O(h^6) &= 0, \end{aligned} \quad (10)$$

where $\mathbf{X}_{mn}^{(j)}$, $\mathbf{Y}_{mn}^{(j)}$, $j = 0, 2, 4$, are lengthy vector quantities involving the field expansion coefficients p_{mn} , q_{mn} , $a_l^{(j)}$, $a_{mn}^{(j)}$, $b_{mn}^{(j)}$, $j = 0, 2, 4$, and the SSHVs. Keeping terms up to $O(h^4)$, setting each $\mathbf{X}_{mn}^{(j)}$, $\mathbf{Y}_{mn}^{(j)}$ in (10) equal to zero, and grouping the

resulting equations in pairs of zeroth, second and fourth order, respectively, we get

$$\begin{aligned}\mathbf{X}_{mn}^{(0)} &= 0, \mathbf{Y}_{mn}^{(0)} = 0, \\ \mathbf{X}_{mn}^{(2)} &= 0, \mathbf{Y}_{mn}^{(2)} = 0, \\ \mathbf{X}_{mn}^{(4)} &= 0, \mathbf{Y}_{mn}^{(4)} = 0.\end{aligned}\quad (11)$$

For each of the above six equations we take two dot-products as follows: first, we multiply each equation by $\mathbf{B}_{uv}^* \sin \theta d\theta d\varphi$ (the asterisk denoting complex conjugation) and integrate from $\theta = 0$ to π and from $\varphi = 0$ to 2π . Second, we multiply by $\mathbf{C}_{uv}^* \sin \theta d\theta d\varphi$ and again perform the integration with the same limits. Making use of the orthogonality relations of SSHVs, each vector equation yields two scalar linear equations, and the three pairs (11) are finally transformed into three respective linear systems, each one involving four infinite sets of equations, i.e.,

$$\begin{aligned}\sum_{l=1}^{\infty} c_{mnl} j_n(x_l) a_l^{(j)} - h_n(x_0) a_{mn}^{(j)} &= Y_{1,mn}^{(j)}, \\ \sum_{l=1}^{\infty} \frac{a_l^{(j)}}{x_l} \left[d_{mnl} j_n^d(x_l) + \frac{\bar{w}_{mnl}}{\lambda_l} j_n(x_l) \right] - \frac{h_n^d(x_0)}{x_0} b_{mn}^{(j)} \\ &= Y_{2,mn}^{(j)}, \\ \sum_{l=1}^{\infty} \tau_l d_{mnl} j_n(x_l) a_l^{(j)} - h_n(x_0) b_{mn}^{(j)} &= Y_{3,mn}^{(j)}, \\ \sum_{l=1}^{\infty} \tau_l c_{mnl} \frac{j_n^d(x_l)}{x_l} a_l^{(j)} - \frac{h_n^d(x_0)}{x_0} a_{mn}^{(j)} &= Y_{4,mn}^{(j)}.\end{aligned}\quad (12)$$

In (12), $x_0 = k_0 c_0$ is the normalized wavenumber, $x_l = \tau_l x_0$, $z_n^d(x) \equiv z_n(x) + x z_n'(x)$, $z_n = j_n, h_n$, and the prime denotes differentiation with respect to the argument. Eqs (12) are obtained after lengthy algebra and comprise, upon truncation, the linear system of j -th order, having the form $\mathbf{A} \mathbf{v}^{(j)} = \mathbf{Y}^{(j)}$. The expressions of the right hand sides (RHSs) of (12) are given in the Appendix, where it can be seen that $\mathbf{Y}^{(0)}$ depends on q_{mn} and p_{mn} , $\mathbf{Y}^{(2)}$ depends on q_{mn} , p_{mn} , $a_l^{(0)}$, $a_{mn}^{(0)}$, $b_{mn}^{(0)}$, while $\mathbf{Y}^{(4)}$ depends on q_{mn} , p_{mn} , $a_l^{(j)}$, $a_{mn}^{(j)}$, $b_{mn}^{(j)}$, $j = 0, 2$. Therefore, the systems are solved successively, i.e., the zeroth order system is solved first, $a_l^{(0)}$, $a_{mn}^{(0)}$, $b_{mn}^{(0)}$ are found and then used to generate the RHS of the second order system. Solution of the latter yields $a_l^{(2)}$, $a_{mn}^{(2)}$, $b_{mn}^{(2)}$, which in turn are used—along with $a_l^{(0)}$, $a_{mn}^{(0)}$, $b_{mn}^{(0)}$ —to generate the RHS of the fourth order system. Solution of the latter yields $a_l^{(4)}$, $a_{mn}^{(4)}$, $b_{mn}^{(4)}$. We point out that system matrix \mathbf{A} is the same for every system order, and needs to be assembled only once in the computer program.

Once $a_l^{(j)}$, $a_{mn}^{(j)}$, $b_{mn}^{(j)}$ are known, the field expansion coefficients are obtained by (9). Then, using the scattered far field $\mathbf{E}^s = e^{jk_0 r} / (k_0 r) [f_\theta(\theta, \varphi) \mathbf{e}_\theta + f_\varphi(\theta, \varphi) \mathbf{e}_\varphi]$, where f_θ, f_φ are the components of the scattering amplitude that depend on $a_{mn}^{(0),(2),(4)}$, $b_{mn}^{(0),(2),(4)}$, the bistatic radar cross section (RCS)

$\sigma(\theta, \varphi)$ can be expressed in the form

$$\begin{aligned}\sigma(\theta, \varphi) \\ = \sigma^{(0)}(\theta, \varphi) \left[1 + g^{(2)}(\theta, \varphi) h^2 + g^{(4)}(\theta, \varphi) h^4 + O(h^6) \right].\end{aligned}\quad (13)$$

In (13) $\sigma^{(0)}(\theta, \varphi)$ corresponds to the RCS of the unperturbed sphere, while the correction terms $g^{(2),(4)}(\theta, \varphi)$ depend on $a_{mn}^{(0),(2),(4)}$, $b_{mn}^{(0),(2),(4)}$ and are independent of h . The expressions $\sigma^{(0)}(\theta, \varphi)$, $g^{(2),(4)}(\theta, \varphi)$ can be readily computed, and once available, can be used for fast RCS computations via (13) for many different values of h . Similarly, the total scattering cross section Q_t is expressed as

$$Q_t = Q_t^{(0)} + Q_t^{(2)} h^2 + Q_t^{(4)} h^4 + O(h^6), \quad (14)$$

where

$$\begin{aligned}Q_t^{(0)} &= \frac{\lambda_0^2}{\pi} \sum_{\substack{m=-\infty \\ n=|m|}}^{\infty} (|a_{mn}^{(0)}|^2 + |b_{mn}^{(0)}|^2), \\ Q_t^{(2)} &= \frac{\lambda_0^2}{\pi} 2 \sum_{\substack{m=-\infty \\ n=|m|}}^{\infty} \text{Re}(a_{mn}^{(0)*} a_{mn}^{(2)} + b_{mn}^{(0)*} b_{mn}^{(2)}), \\ Q_t^{(4)} &= \frac{\lambda_0^2}{\pi} \sum_{\substack{m=-\infty \\ n=|m|}}^{\infty} \left[|a_{mn}^{(2)}|^2 + |b_{mn}^{(2)}|^2 \right. \\ &\quad \left. + 2\text{Re}(a_{mn}^{(0)*} a_{mn}^{(4)} + b_{mn}^{(0)*} b_{mn}^{(4)}) \right].\end{aligned}\quad (15)$$

In (15), $\lambda_0 = 2\pi/k_0$ is the free space wavelength. It should be noted that the perturbation analysis applied in (2)–(4), the composition of the RHS in (12), and the derivation of (13), (14), is exact up to the order of h^4 (see also Appendix). This means that the present method, through (14), serves as an accurate and fast tool for revealing the resonant scattering characteristics of anisotropic spheroids.

B. Oblate Spheroid

For the oblate spheroid, $a_l^{(j)}$, $a_{mn}^{(j)}$, $b_{mn}^{(j)}$ are again obtained by the linear systems (12), but $-h^2$ is used in place of h^2 for the calculation of a_l , a_{mn} , b_{mn} in (9), as well as in the RCS computations (13), (14).

III. VALIDATION AND PERFORMANCE

We hereby demonstrate the validity, accuracy and efficiency of the proposed perturbation-based DEM method, by computing the normalized bistatic RCS σ/λ_0^2 in dB, for various spheroidal anisotropic configurations. We begin with the verification of DEM for prolate uniaxial spheroids, and then proceed to the oblate case. To validate DEM, we employ ADDA code [29], a particular version of DDA, which is capable of computing the RCS of uniaxial scatterers. The incident plane wave $\mathbf{E}^{\text{inc}} = \mathbf{e}_x e^{ik_0 z}$ is considered in our computations. In what follows, the permittivity tensor (1) will be displayed as a set $\epsilon/\epsilon_0 = \{\epsilon_{or}, \epsilon_{or}, \epsilon_{er}\}$.

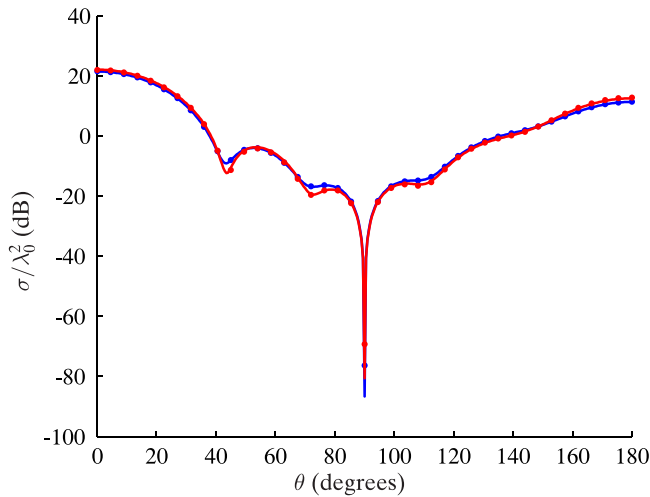


Fig. 2. Bistatic RCS for uniaxial prolate spheroids with $x_0 = 1.5\pi$, $\epsilon/\epsilon_0 = \{3, 3, 1\}$ and $\varphi = 0^\circ$. Curves: DEM; dots: ADDA. Blue curve/dots: $h = 0.1$; red curve/dots: $h = 0.3$.

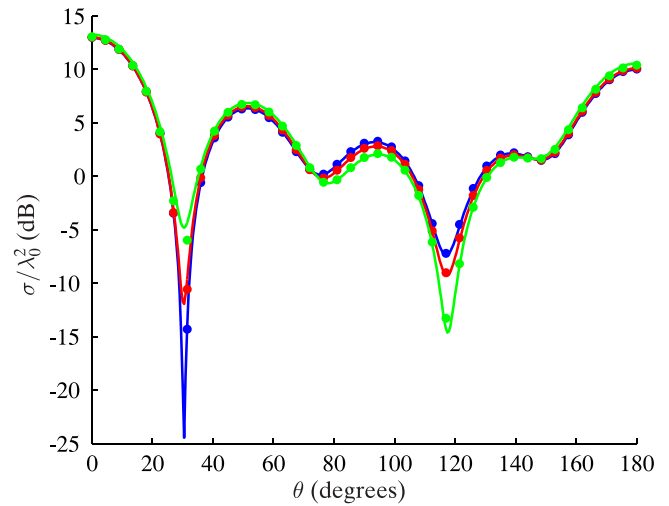


Fig. 3. Bistatic RCS for uniaxial oblate spheroids with $x_0 = 1.3\pi$, $\epsilon/\epsilon_0 = \{4, 4, 2.5\}$ and $\varphi = 0^\circ$. Curves: DEM; dots: ADDA. Blue curve/dots: $h = 0.1$; red curve/dots: $h = 0.2$; green curve/dots: $h = 0.3$.

We begin the validation directly with anisotropic spheroids. The isotropic case—obtained by (1) by letting $\epsilon_o \equiv \epsilon_e$ —is not considered at all herein. The reason is that DEM yields precisely the same numerical values of $g^{(2)}$, $g^{(4)}$ appearing in (13), with the ones appearing in [20, Tables III, IV]. Therefore, all conclusions drawn in [20] regarding the validity of the perturbation method for isotropic spheroidal scatterers, apply here as well. Here we focus on the anisotropic response which constitutes the main novel point of this work.

In Fig. 2 we plot the RCS for uniaxial prolate spheroids and two different values of eccentricity h . The values of parameters are gathered in Figure’s caption. DEM and ADDA overlap excellently, even at the large draught appearing at $\theta = 90^\circ$, thus verifying the accuracy of the results. The small deviation in RCS versus h , i.e., from $h = 0.1$ to $h = 0.3$, is well captured by both methods, as it is depicted around $\theta = 45^\circ$ or around $\theta = 70^\circ$. In order to distinguish the small deviations around $\theta = 45^\circ$ and $\theta = 70^\circ$ with ADDA, we need to initialize it with many dipoles per wavelength (DPL). In the present and all subsequent examples, ADDA is initialized as follows: first, we use 128 DPL to ensure convergence. To model the spheroid, we use the default ellipsoid shape by defining the ratios $y/x = 1$, $z/x = 1/\sqrt{1-h^2}$ for the prolate spheroid, and $y/x = 1$, $z/x = 1/\sqrt{1+h^2}$ for the oblate spheroid. The equivalent radius needed in ADDA is set equal to $c_0(1-h^2)^{1/3}$ for the prolate and equal to $c_0(1+h^2)^{1/3}$ for the oblate spheroid, with c_0 defined in microns. In our computations we set $c_0 = 1 \mu\text{m}$, while the incident wavelength is set equal to $2\pi c_0/x_0$. Finally, the uniaxial tensor is defined through the anisotropic refractive index by defining the three elements as $\{\sqrt{\epsilon_{or}}, \sqrt{\epsilon_{or}}, \sqrt{\epsilon_{er}}\}$. All calculations were performed on a Dell Precision 2.26 GHz double quad-core Xeon equipped machine. The computational performance of ADDA is 900 s/1113 s for $h = 0.1/h = 0.3$. CPU time for DEM is only 3.2 s for $h = 0.1$. When $h = 0.3$, we do not need to repeat the execution of the whole program for DEM, but since $g^{(2)}$, $g^{(4)}$ in (13) are known from the first run (the one for $h = 0.1$), the RCS for $h = 0.3$ is

obtained immediately by the closed-form formula (13) in zero time. Thus, the total CPU time for the two plots in Fig. 2 using ADDA is 2013 s, while the total CPU time for DEM is 3.2 s. Obviously, the superiority of DEM is revealed when one needs to compute RCS for many different values of h . Nonetheless, even a single run using DEM is much faster than a single run using ADDA.

The prolate case of Fig. 2 does not present strong variations in RCS due to changing h . A more illustrative example is provided by the uniaxial oblate spheroid considered in Fig. 3. Here, even small changes in h (from $h = 0.1$ to $h = 0.3$) result in notable variations in RCS, and one can see how eccentricity affects RCS. DEM/ADDA are in excellent agreement for all h used. RCS plots show that the first draught at $\theta = 30^\circ$ starts to disappear when h increases, and a second one just before $\theta = 120^\circ$ starts to emerge. Obviously, both DEM/ADDA capture this behavior, which further verifies the accuracy of DEM. CPU time for ADDA is 1164/1524/1624 s for $h = 0.1/h = 0.2/h = 0.3$ —i.e., time increases when h increases. CPU time for DEM is only 2.5 s for $h = 0.1$. Total CPU time for all three plots in Fig. 3 using ADDA is 4312 s, while total CPU time for DEM is again 2.5 s, as explained above.

To conclude about the applicability domain of DEM, we further investigate its validation/performance by plotting in Fig. 4 the normalized back RCS $\sigma_b/\lambda_0^2 \equiv \sigma(\pi, 0)/\lambda_0^2$ versus x_0 , for an uniaxial oblate spheroid and various values of h . In the plots of Fig. 4, the total number of points for x_0 using DEM is 121 (i.e., $x_0 \in [1, 7]$ with a step of 0.05), while for ADDA we have used a step of 0.1, i.e., 61 points, due to extremely large CPU time required by it. As it can be seen, the precise locations of the draughts and peaks are not fixed, but are sensitive to the small changes of h . For small values of h , i.e., for $h = 0.15, 0.25, 0.35$, DEM and ADDA are in excellent agreement. When h increases further, DEM starts to deviate, but this deviation is pronounced when x_0 is large and located around a draught. For instance, when $h = 0.5$, the agreement is

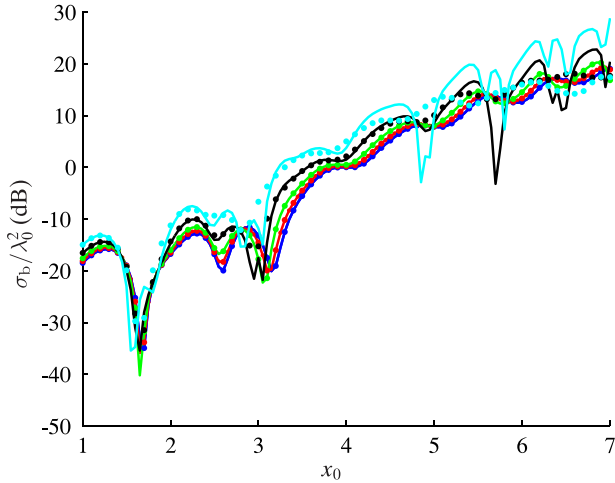


Fig. 4. Back RCS versus x_0 for uniaxial oblate spheroids with $\epsilon_r/\epsilon_0 = \{2.2, 2.2, 3.5\}$. Curves: DEM; dots: ADDA. Blue curve/dots: $h = 0.15$; red curve/dots: $h = 0.25$; green curve/dots: $h = 0.35$; black curve/dots: $h = 0.5$; cyan curve/dots: $h = 0.7$.

good for a large range of x_0 , but it deteriorates around $x_0 = 3$ and for $x_0 > 5.5$ where multiple draughts are present. However, it is important to stress that for small values of x_0 , the agreement between DEM and ADDA is very good, even the first draught below $x_0 = 2$ is captured well. In the context of nanoantenna design—see Section IV—this observation allows us to apply DEM even for h up to 0.5, since the nanoantenna operates in subwavelength regime. When $h = 0.7$, the disagreement between DEM and ADDA is evident, especially for $x_0 > 4$, since the asymptotic terms used in (13) are not sufficient to accurately resolve the solution for higher values of h . CPU time for DEM to produce a single curve is 145 s, and it is the same for all values of h used in Fig. 4. The indicative CPU time for ADDA for the cases $h = 0.15, 0.25, 0.35$ is 19079 s ≈ 5.3 h using 64 DPL. When $h = 0.5$ or 0.7, we had to increase DPL to 128 to assure convergence, then the CPU time was increased to 242867 s ≈ 67.5 h when $h = 0.5$, and to 375357 s ≈ 104.3 h when $h = 0.7$. Similar observations on accuracy/performance also hold for Q_t through (14), and are not given here for brevity. Since the perturbation parameter in (13), (14) is h , DEM is also valid for higher values of x_0 , as long as h is kept small. To show this, we compute σ_b/λ_0^2 (dB) = 19.58, 19.53, 20.92, and $Q_t/\lambda_0^2 = 7.23, 7.85, 18.91$ for $x_0 = 7.5, 8, 10$, respectively, by DEM, while the respective results by ADDA are σ_b/λ_0^2 (dB) = 19.54, 19.54, 20.9 and $Q_t/\lambda_0^2 = 7.28, 7.9, 18.96$. Summarizing, as long as h is kept small up to 0.35, or up to 0.5 in combination with small x_0 , the perturbation method has excellent performance for revealing the scattering characteristics of anisotropic spheroids, especially for multiple calculations over h .

IV. ENGINEERING ANISOTROPIC NANOANTENNAS

In this Section we introduce anisotropy and non sphericity to tailor the location of Kerker points, and thus optimize the operation of nanoantennas at desired wavelengths. Realistic dispersive uniaxial anisotropic materials, like TiO_2 and ZnGeP_2 , may

be used to form nanoantennas. These semiconductor crystals exhibit high ordinary/extraordinary refractive indices, throughout the visible range. For instance, TiO_2 is positive uniaxial (PU) ($\epsilon_{er} > \epsilon_{or}$) and presents an indicative average ordinary relative permittivity $\epsilon_{or} = 7.0668$ and an average extraordinary relative permittivity $\epsilon_{er} = 8.8027$ at 430 nm–700 nm [23, p. 33.66]. In this wavelength regime, TiO_2 has an average AR = 0.109. ZnGeP_2 is PU and exhibits even higher indices that enhance the unidirectional properties, with indicative average values $\epsilon_{or} = 15.994$, $\epsilon_{er} = 17.847$, and AR = 0.0548 at 400 nm–700 nm [23, p. 33.66]. In what follows, we do not use these average values in the calculations, but we employ the dispersive relations $\epsilon_{or} = \epsilon_{or}(\lambda_0)$ and $\epsilon_{er} = \epsilon_{er}(\lambda_0)$ given in [23], with the argument λ_0 omitted throughout for simplicity.

In subwavelength regime, EM scattering is characterized by various magnetic/electric resonances. For an isotropic spherical nanoparticle, the MD/ED resonance corresponds to the response of the expansion coefficient $a_{11}^{(0)}/b_{11}^{(0)}$ in the calculation of Q_t [34]. Similarly, the magnetic/electric quadrupolar (MQ)/(EQ) resonance corresponds to the response of $a_{12}^{(0)}/b_{12}^{(0)}$, and so on. Obviously, for isotropic-dielectric spherical particles, the stimulating plane wave can impinge along z -direction without violating any generality, and therefore $m = 1$ always [31], for all orders of resonances ($n = 1, 2, \dots$). This is not the case for spherical uniaxial nanoparticles, or spheroidal isotropic/anisotropic ones, since anisotropy—through its optical axis—and non sphericity—through eccentricity—cancel any symmetry along θ -direction. This means that the magnetic/electric resonances, are due to the response of $a_{mn}^{(0)}/b_{mn}^{(0)}$, where now $m = -\infty, \infty$. For instance, the MQ resonance in an uniaxial sphere is due to $n = 2, m = 0, \pm 1, \pm 2$. This fact differentiates and generalizes our study from the existing ones mentioned in Introduction, which concern dielectric spheres. On top of that, when nanosphere becomes nanospheroid, the magnetic and electric resonances will be described by the correction terms $a_{mn}^{(2),(4)}$ and $b_{mn}^{(2),(4)}$, respectively, in the calculation of Q_t —see (14), (15).

In what follows, the EM scattering problem is stimulated by an incident plane wave of the form $\mathbf{E}^{\text{inc}} = \mathbf{e}_x e^{ik_0 z}$ (therefore the plane wave is impinging at 0° with respect to positive z semi-axis), where \mathbf{E}^{inc} is normal to the yz -plane of incidence (TE incidence). In Fig. 5, the solid curves (with respect to left axis) depict spectra for subwavelength 100 nm radius ZnGeP_2 nanosphere, by calculating the normalized Q_t/λ_0^2 over the visible and near-infrared (IR). The blue/solid curve corresponds to full-wave calculation of Q_t/λ_0^2 , i.e., all m, n terms in (15) are used, while the remaining solid curves (red, green, black) correspond to Q_t/λ_0^2 due to separate MD, ED and MQ terms only (i.e., using only the $a_{m,1}^{(0)}, b_{m,1}^{(0)}$ and $a_{m,2}^{(0)}$ terms, respectively, in (15)). The dashed curves (with respect to right axis) depict σ_b/λ_0^2 in dB. The blue/dashed curve corresponds to a full-wave calculation, while the red/dashed curve corresponds to a calculation due to both MD/ED terms (i.e., both $a_{m,1}^{(0)}, b_{m,1}^{(0)}$ contribute in (13)). Obviously, the various resonances are well pronounced for ZnGeP_2 in the full-wave solution of Q_t/λ_0^2 , due to its high $\epsilon_{or}/\epsilon_{er}$. The first Kerker condition point [35] appears at the

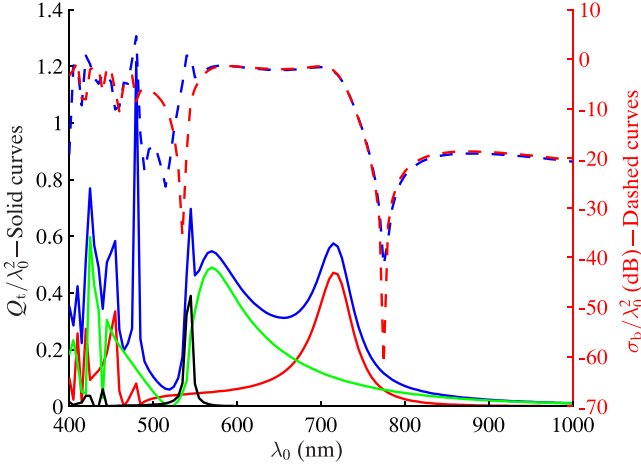


Fig. 5. Resonances of an 100 nm radius ZnGeP₂ sphere. Left axis/solid curves: Q_t/λ_0^2 vs λ_0 ; blue: full-wave solution; red: MD term; green: ED term; black: MQ term. Right axis/dashed curves: σ_b/λ_0^2 vs λ_0 ; blue: full-wave solution; red: both MD/ED terms.

first intersection between MD and ED curves, for Q_t/λ_0^2 , as we move from IR towards blue, i.e., at 775 nm. As can be seen from right axis plots in Fig. 5, both the full-wave and MD/ED terms solutions for σ_b/λ_0^2 indicate a minimum, which coincides with 775 nm where the aforementioned MD/ED intersection takes place. Since σ_b/λ_0^2 is minimum, forward unidirectional scattering occurs. This particular λ_0 is referred as the first Kerker wavelength. The second σ_b/λ_0^2 minimum from MD/ED terms, observed at 535 nm (red/dashed curve), does not correspond to a forward unidirectional state, since coherent contribution takes place from other higher order resonances. Indeed, the full-wave solution for σ_b/λ_0^2 does not depict a draught there. The second Kerker condition point appears at the second intersection between MD and ED curves. For ZnGeP₂, this is observed at 670 nm (second Kerker wavelength). At this point, the normalized forward RCS $\sigma_f/\lambda_0^2 \equiv \sigma(0,0)/\lambda_0^2$ yields a minimum.

ZnGeP₂ presents higher indices than TiO₂, but the latter exhibits higher AR. In Fig. 6 we study the influence of AR on subwavelength resonances. We consider two cases: the PU case defined above, and the negative uniaxial (NU) case ($\epsilon_{er} < \epsilon_{or}$). To this end, we begin with the original ZnGeP₂ being PU, whose dispersive relations for $(\epsilon_{or}, \epsilon_{er})$ are given in [23]. Then, to increase the AR and keep the PU property, we introduce the cases $(\epsilon_{or} - 2, \epsilon_{er})$, $(\epsilon_{or} - 4, \epsilon_{er})$. This means that the combination $(\epsilon_{or} - 4, \epsilon_{er})$ has increased AR as compared to the original $(\epsilon_{or}, \epsilon_{er})$, still both cases maintain the PU property. Similarly, the effect of NU property is examined by introducing the cases $(\epsilon_{or} + 2, \epsilon_{er})$, $(\epsilon_{or} + 4, \epsilon_{er})$. These selections ensure that $\epsilon_{er} < \epsilon_{or}$ always. Fig. 6 focuses on the influence of AR on MD/ED resonances. It is clear that a PU crystal with increased AR enables a blue shift of both MD/ED resonances, while a high AR NU crystal causes shifts towards IR. On the contrary, the MD/ED resonances of an equivalent dielectric will be observed between PU and NU states ($\epsilon_{er} = \epsilon_{or}$). These characteristics reveal that the introduction of a high AR PU natural crystal, supports the shift of Kerker points inside the

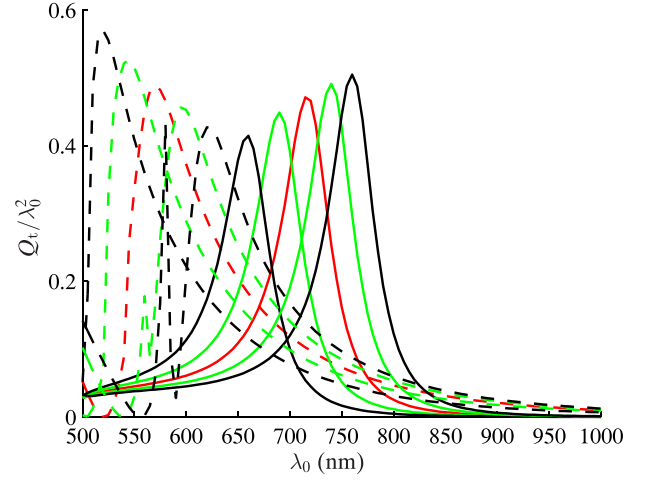


Fig. 6. MD/ED resonances of an 100 nm radius ZnGeP₂ sphere due to different ARs. Group I/solid curves: MD resonances; group II/dashed curves: ED resonances. For each group: red: original ZnGeP₂ with $(\epsilon_{or}, \epsilon_{er})$. Shifts towards blue: PU case; green: $(\epsilon_{or} - 2, \epsilon_{er})$; black: $(\epsilon_{or} - 4, \epsilon_{er})$. Shifts towards IR: NU case; green: $(\epsilon_{or} + 2, \epsilon_{er})$; black: $(\epsilon_{or} + 4, \epsilon_{er})$.

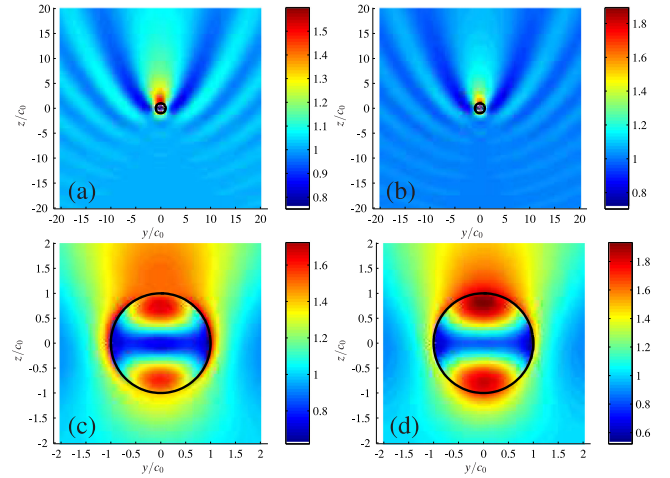


Fig. 7. Total $|\mathbf{E}|$ (V/m) on yz -plane for the $c_0 = 100$ nm radius ZnGeP₂ sphere, using DEM. The incident plane wave is impinging at 0° with respect to positive z semi-axis. (a) Original ZnGeP₂ with $(\epsilon_{or}, \epsilon_{er})$, stimulated at $\lambda_0 = 775$ nm (first Kerker wavelength); (b) PU case with $(\epsilon_{or} - 4, \epsilon_{er})$, stimulated at $\lambda_0 = 708$ nm (first Kerker wavelength); (c) focused image of (a); (d) focused image of (b).

visible through material tuning, offering more design flexibility in nanoscale, a case which is not achievable with conventional isotropic dielectrics. Indeed, the first/second Kerker point for the original ZnGeP₂, is observed at 775 nm/670 nm (intersections of red solid/dashed curves). The first/second Kerker point using the PU case with $(\epsilon_{or} - 4, \epsilon_{er})$, is observed at 708 nm/620 nm (intersections of black solid/dashed curves). To verify the forward unidirectional behavior of the anisotropic nanoantennas examined in Fig. 6, in Figs 7(a), (b) we plot the total $|\mathbf{E}| = \sqrt{|E_r|^2 + |E_\theta|^2 + |E_\varphi|^2}$ on yz -plane, up to twenty radii away, for the original ZnGeP₂ with $(\epsilon_{or}, \epsilon_{er})$, and for the enhanced AR PU case of $(\epsilon_{or} - 4, \epsilon_{er})$, respectively. These plots were obtained by DEM. The incident plane wave is stimulated at the respective first Kerker wavelengths, as observed in Fig. 6 above.

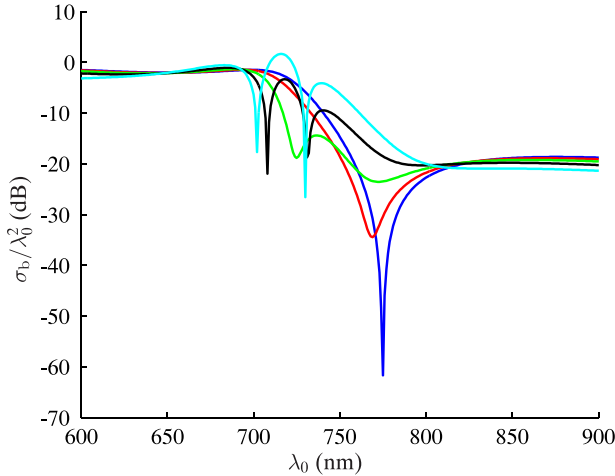


Fig. 8. First Kerker minima (using both MD/ED terms) of a prolate ZnGeP₂ spheroid having semi-major axis $c_0 = 100$ nm, due to different h . Blue: $h = 0$ (sphere); red: $h = 0.2$; green: $h = 0.3$; black: $h = 0.4$; cyan: $h = 0.5$.

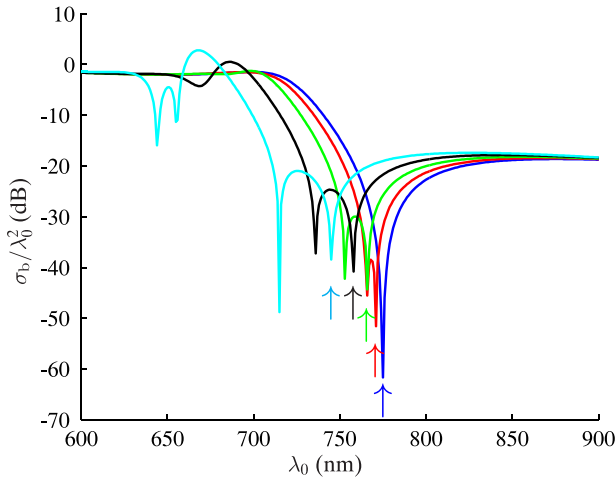


Fig. 9. First Kerker minima (using both MD/ED terms) of an oblate ZnGeP₂ spheroid having semi-major axis $b_0 = 100$ nm, due to different h . Arrows indicate the location of first Kerker minima. Blue: $h = 0$ (sphere); red: $h = 0.2$; green: $h = 0.3$; black: $h = 0.4$; cyan: $h = 0.5$.

In Figs 7(c), (d) we present focused images of the same setups, around the nanoantennas, where the coherent MD/ED response is evident from the field patterns.

Next, we examine how the geometry of the nanoantenna affects its characteristics. Kerker points can be further shifted towards blue, by introducing spheroidal nanoparticles. In the following, we illustrate the qualitative alteration of the first Kerker minimum, as the nanoparticle deviates from sphericity, by plotting σ_b/λ_0^2 vs λ_0 , for various values of h . This is done in Figs 8 and 9 where we study prolate/oblate spheroids. The curves have been obtained using both MD/ED terms. First Kerker minima are indicated by the sharp draughts. To clearly illustrate the effect of h on these resonances, we focus on the range 600 nm–900 nm. In order to avoid altering the physics due to different sizes, for a fair comparison between prolate/oblate shape, the larger dimension of each particle must not change. Therefore, for the prolate case we keep the semi-major axis

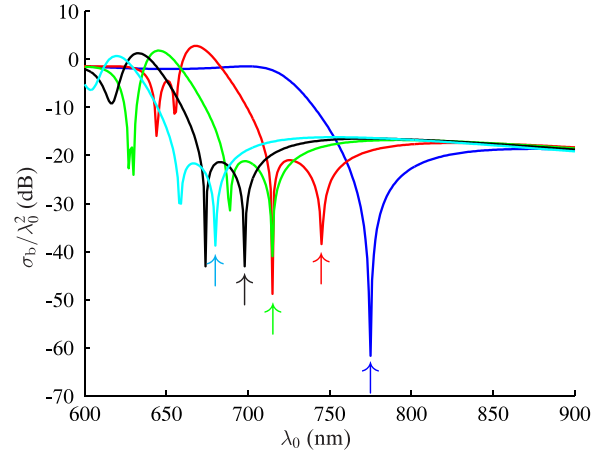


Fig. 10. First Kerker minima (using both MD/ED terms) of an oblate ZnGeP₂ spheroid having semi-major axis $b_0 = 100$ nm and $h = 0.5$, due to different ARs. Arrows indicate the location of first Kerker minima. Red: original ZnGeP₂ with $(\epsilon_{or}, \epsilon_{er})$ (same result with Fig. 9/cyan curve); green: $(\epsilon_{or} - 2, \epsilon_{er})$; black: $(\epsilon_{or} - 3, \epsilon_{er})$; cyan: $(\epsilon_{or} - 4, \epsilon_{er})$. Blue: original ZnGeP₂ with $(\epsilon_{or}, \epsilon_{er})$ and $h = 0$ (sphere—same result with Fig. 9/blue curve).

$c_0 = 100$ nm (i.e., equal to the radius of the original sphere), and its semi-minor axis changes as $b_0 = c_0\sqrt{1 - h^2}$. For the oblate case, we keep the semi-major axis $b_0 = 100$ nm, and the semi-minor axis changes as $c_0 = b_0/\sqrt{1 + h^2}$.

From Fig. 8 it is evident that, as h increases, the prolate shape cannot guarantee the elimination of the backscattered power, i.e., no deep draughts exist. Contrariwise, the oblate spheroid, as Fig. 9 reveals, allows for deep draughts (indicated by vertical arrows) with significant reduction of backscattered power, moreover, these draughts are blue shifted as h increases. For instance, the oblate spheroid with $h = 0.4$ has a shifted (with respect to the unperturbed sphere) draught at 758 nm, while the $h = 0.5$ case yields a draught at 745 nm. The other draughts, for instance the one appearing at 715 nm when $h = 0.5$, do not correspond to a Kerker minimum, since coherent contribution takes place from other higher order resonances. Fig. 10 further shows Kerker minima for an oblate spheroid with $h = 0.5$, but now AR is enhanced to show how it affects these minima. We introduce the cases $(\epsilon_{or} - 2, \epsilon_{er})$, $(\epsilon_{or} - 3, \epsilon_{er})$, $(\epsilon_{or} - 4, \epsilon_{er})$, as we did in Fig. 6, and plot σ_b/λ_0^2 . Obviously, the deep draughts are further shifted towards blue, entering the red zone of 620 nm–750 nm, as AR increases. Higher values of h than those examined in this Section cannot be used in the present development, since more asymptotic terms are needed in the final expansion of (14). Yet, in combination with anisotropy, a high aspect ratio oblate spheroid (nanodisk) may allow for stronger shifts inside the visible. To use higher values of h and support anisotropic materials, the development of another full-wave method is required, since the formulation offered in [18], [20], is valid only for isotropic spheroids. Concluding, the overall optimization of the nanoantenna design is based on modifying both geometry and anisotropy, a combination that allows for stronger shifts of first Kerker minima towards blue, thus tailoring the unidirectional properties of the nanoantenna, rendering it wavelength dependent.

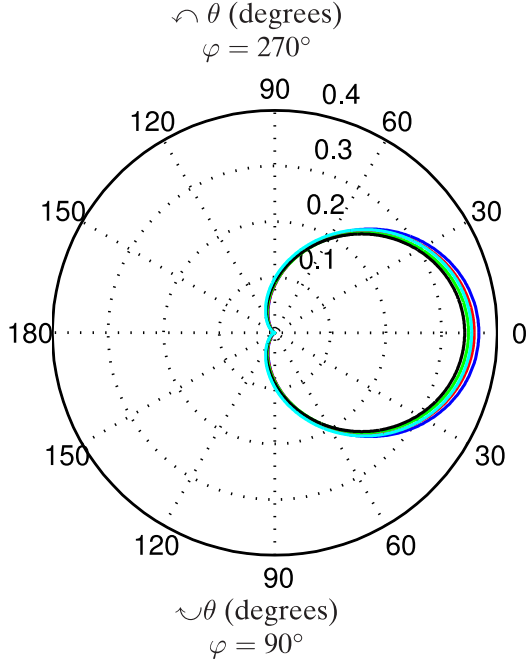


Fig. 11. Bistatic RCS σ/λ_0^2 vs θ on $\{x=0, y>0\}$ plane ($\varphi=90^\circ$) and on $\{x=0, y<0\}$ plane ($\varphi=270^\circ$), for the oblate ZnGeP₂ spheroids examined in Fig. 9. The incident plane wave is impinging at 0° with respect to positive z semi-axis, and is stimulated at Kerker wavelengths, as indicated in Fig. 9. Blue: $h=0/\lambda_0=775$ nm (sphere); red: $h=0.2/\lambda_0=771$ nm; green: $h=0.3/\lambda_0=766$ nm; black: $h=0.4/\lambda_0=758$ nm; cyan: $h=0.5/\lambda_0=745$ nm.

Since the nanoantenna is non spherical and anisotropic, the direction of plane wave incidence plays a role in Kerker response. Keeping the TE plane wave incidence as above, but changing its direction 90° with respect to positive z semi-axis, the first Kerker minima due to a prolate spheroid are again blue shifted, but still significant backscattered power exists as in the aforementioned prolate case of Fig. 8, where the incidence was defined at 0° with respect to positive z semi-axis. Yet, another point to mention is that, the TM incidence (\mathbf{E}^{inc} belongs on the yz -plane of incidence) yields slightly different results as compared to the TE incidence examined above, but not significantly different to fundamentally change the scattering response.

Fig. 11 verifies that, if the various oblate anisotropic nanoantennas examined in Fig. 9 are stimulated at their respective Kerker wavelengths, they present forward unidirectional properties with eliminated back scattering. In addition, the radiation wavelength of an oblate nanoantenna can be tuned by geometry and material shaping, as analyzed in Figs 9, 10.

V. CONCLUSION

We investigated the engineering of subwavelength nanoantennas composed of uniaxial nanospheroids, by rigorously developing a fast and accurate perturbation-based DEM, for the EM scattering of a plane wave by a prolate or oblate uniaxial spheroid. The development of anisotropic nanoantennas permits the shift of Kerker points several tens of nm towards blue, as compared to all-dielectric nanoantennas, and enables to tune the wavelength of the forward directional radiation within the visible. This is achieved by tailoring the material and the geometry

of the nanoparticle that forms the nanoantenna. Material shaping is introduced by dispersive uniaxial semiconductor crystals, like TiO₂ or ZnGeP₂, featuring high ordinary/extraordinary refractive indices throughout the visible. Positive uniaxial crystals with enhanced anisotropy ratio, give rise to strong shifts towards blue, as compared to conventional dielectrics. Additionally, non sphericity perturbs the precise locations of Kerker points, and it is shown that oblate geometry shaping allows for further shift of Kerker points towards blue, keeping the forward unidirectional operation of the nanoantenna.

APPENDIX

The RHS terms in (12) are given by

$$Y_{1,mn}^{(0)} = q_{mn} j_n(x_0), \quad Y_{2,mn}^{(0)} = p_{mn} j_n^d(x_0)/x_0, \quad (\text{A.1})$$

$$\begin{aligned}
Y_{1,mn}^{(2)} &= \sum_{s=n, n\pm 2} \frac{\bar{E}_{ms}}{\bar{E}_{mn}} \left[q_{ms} B_{1,s}^{(2)}(x_0) + a_{ms}^{(0)} B_{3,s}^{(2)}(x_0) \right. \\
&\quad \left. - \sum_{l=1}^{\infty} a_l^{(0)} c_{m sl} B_{1,s}^{(2)}(x_l) \right] \frac{N_{1,msn}}{n(n+1)I_{mnn}} - \sum_{s=n\pm 1} \frac{\bar{E}_{ms}}{\bar{E}_{mn}} \\
&\quad \times \left\{ p_{ms} \Delta_{1,s}^{(2)}(x_0) + b_{ms}^{(0)} \Delta_{3,s}^{(2)}(x_0) - \sum_{l=1}^{\infty} a_l^{(0)} \left[d_{m sl} \Delta_{1,s}^{(2)}(x_l) \right. \right. \\
&\quad \left. \left. + \frac{\bar{w}_{m sl}}{\lambda_l} \Gamma_{1,s}^{(2)}(x_l) \right] \right\} \frac{N_{2,msn}}{n(n+1)I_{mnn}} + \sum_{s=n\pm 1} \frac{\bar{E}_{ms}}{\bar{E}_{mn}} \\
&\quad \times \left\{ s(s+1) p_{ms} \frac{j_s(x_0)}{x_0} + s(s+1) b_{ms}^{(0)} \frac{h_s(x_0)}{x_0} \right. \\
&\quad \left. - \sum_{l=1}^{\infty} a_l^{(0)} \left[s(s+1) d_{m sl} \frac{j_s(x_l)}{x_l} + \frac{\bar{w}_{m sl}}{\lambda_l} j_s'(x_l) \right] \right\} \\
&\quad \times \frac{imI_{5,msn}}{n(n+1)I_{mnn}}, \\
Y_{2,mn}^{(2)} &= \sum_{s=n, n\pm 2} \frac{\bar{E}_{ms}}{\bar{E}_{mn}} \left\{ p_{ms} \Delta_{1,s}^{(2)}(x_0) \right. \\
&\quad \left. + b_{ms}^{(0)} \Delta_{3,s}^{(2)}(x_0) - \sum_{l=1}^{\infty} a_l^{(0)} \left[d_{m sl} \Delta_{1,s}^{(2)}(x_l) + \frac{\bar{w}_{m sl}}{\lambda_l} \Gamma_{1,s}^{(2)}(x_l) \right] \right\} \\
&\quad \times \frac{N_{1,msn}}{n(n+1)I_{mnn}} - \sum_{s=n\pm 1} \frac{\bar{E}_{ms}}{\bar{E}_{mn}} \left[q_{ms} B_{1,s}^{(2)}(x_0) \right. \\
&\quad \left. + a_{ms}^{(0)} B_{3,s}^{(2)}(x_0) - \sum_{l=1}^{\infty} a_l^{(0)} c_{m sl} B_{1,s}^{(2)}(x_l) \right] \frac{N_{2,msn}^*}{n(n+1)I_{mnn}} \\
&\quad + \sum_{s=n, n\pm 2} \frac{\bar{E}_{ms}}{\bar{E}_{mn}} \left\{ s(s+1) p_{ms} \frac{j_s(x_0)}{x_0} + s(s+1) b_{ms}^{(0)} \frac{h_s(x_0)}{x_0} \right. \\
&\quad \left. - \sum_{l=1}^{\infty} a_l^{(0)} \left[s(s+1) d_{m sl} \frac{j_s(x_l)}{x_l} + \frac{\bar{w}_{m sl}}{\lambda_l} j_s'(x_l) \right] \right\} \\
&\quad \times \frac{I_{7,msn}}{n(n+1)I_{mnn}}, \quad (\text{A.2})
\end{aligned}$$

where $B_{1,n}^{(2)}(x) = -xj'_n(x)/2$, $\Gamma_{1,n}^{(2)}(x) = j_n(x)/(2x) - j'_n(x)/2$, $\Delta_{1,n}^{(2)}(x) = j_n(x)/(2x) - j'_n(x)/2 - xj''_n(x)/2$, and for $B_{3,n}^{(2)}$, $\Gamma_{3,n}^{(2)}$, $\Delta_{3,n}^{(2)}$, we replace j_n, j'_n, j''_n with h_n, h'_n, h''_n , respectively. Furthermore,

$$\begin{aligned}
Y_{1,mn}^{(4)} &= Y_{1,mn}^{(2)} + \sum_{s=n,n\pm 2,n\pm 4} \frac{\bar{E}_{ms}}{\bar{E}_{mn}} \left[q_{ms} B_{1,s}^{(4)}(x_0) \right. \\
&+ \left. a_{ms}^{(0)} B_{3,s}^{(4)}(x_0) - \sum_{l=1}^{\infty} a_l^{(0)} c_{msl} B_{1,s}^{(4)}(x_l) \right] \\
&\times \frac{N_{3,msn}}{n(n+1)I_{mnn}} - \sum_{s=n\pm 1} \frac{\bar{E}_{ms}}{\bar{E}_{mn}} \left\{ b_{ms}^{(2)} \Delta_{3,s}^{(2)}(x_0) \right. \\
&- \left. \sum_{l=1}^{\infty} a_l^{(2)} \left[d_{msl} \Delta_{1,s}^{(2)}(x_l) + \frac{\bar{w}_{msl}}{\lambda_l} \Gamma_{1,s}^{(2)}(x_l) \right] \right\} \\
&\times \frac{N_{2,msn}}{n(n+1)I_{mnn}} + \sum_{s=n,n\pm 2} \frac{\bar{E}_{ms}}{\bar{E}_{mn}} \left[a_{ms}^{(2)} B_{3,s}^{(2)}(x_0) \right. \\
&- \left. \sum_{l=1}^{\infty} a_l^{(2)} c_{msl} B_{1,s}^{(2)}(x_l) \right] \frac{N_{1,msn}}{n(n+1)I_{mnn}} \\
&- \sum_{s=n\pm 1,n\pm 3} \frac{\bar{E}_{ms}}{\bar{E}_{mn}} \left\{ p_{ms} \Delta_{1,s}^{(4)}(x_0) + b_{ms}^{(0)} \Delta_{3,s}^{(4)}(x_0) \right. \\
&- \left. \sum_{l=1}^{\infty} a_l^{(0)} \left[d_{msl} \Delta_{1,s}^{(4)}(x_l) + \frac{\bar{w}_{msl}}{\lambda_l} \Gamma_{1,s}^{(4)}(x_l) \right] \right\} \\
&\times \frac{N_{4,msn}^*}{n(n+1)I_{mnn}} + \sum_{s=n\pm 1} \frac{\bar{E}_{ms}}{\bar{E}_{mn}} \left\{ s(s+1) b_{ms}^{(2)} \frac{h_s(x_0)}{x_0} \right. \\
&- \left. \sum_{l=1}^{\infty} a_l^{(2)} \left[s(s+1) d_{msl} \frac{j_s(x_l)}{x_l} + \frac{\bar{w}_{msl}}{\lambda_l} j'_s(x_l) \right] \right\} \\
&\times \frac{imI_{5,msn}}{n(n+1)I_{mnn}} + \sum_{s=n\pm 1,n\pm 3} \frac{\bar{E}_{ms}}{\bar{E}_{mn}} \left\{ s(s+1) p_{ms} \right. \\
&\times \left[\Gamma_{1,s}^{(2)}(x_0) - \frac{j_s(x_0)}{x_0} \right] + s(s+1) b_{ms}^{(0)} \left[\Gamma_{3,s}^{(2)}(x_0) \right. \\
&- \left. \frac{h_s(x_0)}{x_0} \right] - \sum_{l=1}^{\infty} a_l^{(0)} s(s+1) d_{msl} \left[\Gamma_{1,s}^{(2)}(x_l) \right. \\
&- \left. \frac{j_s(x_l)}{x_l} \right] - \left. \sum_{l=1}^{\infty} a_l^{(0)} \frac{\bar{w}_{msl}}{\lambda_l} \left[E_{1,s}^{(2)}(x_l) - j'_s(x_l) \right] \right\} \\
&\times \frac{imI_{6,msn}}{n(n+1)I_{mnn}}, \tag{A.3}
\end{aligned}$$

$$\begin{aligned}
Y_{2,mn}^{(4)} &= Y_{2,mn}^{(2)} - \sum_{s=n\pm 1,n\pm 3} \frac{\bar{E}_{ms}}{\bar{E}_{mn}} \left[q_{ms} B_{1,s}^{(4)}(x_0) \right. \\
&+ \left. a_{ms}^{(0)} B_{3,s}^{(4)}(x_0) \right.
\end{aligned}$$

$$\begin{aligned}
&- \sum_{l=1}^{\infty} a_l^{(0)} c_{msl} B_{1,s}^{(4)}(x_l) \left] \frac{N_{4,msn}}{n(n+1)I_{mnn}} + \sum_{s=n,n\pm 2} \frac{\bar{E}_{ms}}{\bar{E}_{mn}} \right. \\
&\times \left\{ b_{ms}^{(2)} \Delta_{3,s}^{(2)}(x_0) - \sum_{l=1}^{\infty} a_l^{(2)} \left[d_{msl} \Delta_{1,s}^{(2)}(x_l) + \frac{\bar{w}_{msl}}{\lambda_l} \Gamma_{1,s}^{(2)}(x_l) \right] \right\} \\
&\times \frac{N_{1,msn}}{n(n+1)I_{mnn}} - \sum_{s=n\pm 1} \frac{\bar{E}_{ms}}{\bar{E}_{mn}} \left[a_{ms}^{(2)} B_{3,s}^{(2)}(x_0) \right. \\
&- \left. \sum_{l=1}^{\infty} a_l^{(2)} c_{msl} B_{1,s}^{(2)}(x_l) \right] \frac{N_{2,msn}^*}{n(n+1)I_{mnn}} \\
&+ \sum_{s=n,n\pm 2,n\pm 4} \frac{\bar{E}_{ms}}{\bar{E}_{mn}} \left\{ p_{ms} \Delta_{1,s}^{(4)}(x_0) + b_{ms}^{(0)} \Delta_{3,s}^{(4)}(x_0) \right. \\
&- \left. \sum_{l=1}^{\infty} a_l^{(0)} \left[d_{msl} \Delta_{1,s}^{(4)}(x_l) + \frac{\bar{w}_{msl}}{\lambda_l} \Gamma_{1,s}^{(4)}(x_l) \right] \right\} \frac{N_{3,msn}^*}{n(n+1)I_{mnn}} \\
&+ \sum_{s=n,n\pm 2} \frac{\bar{E}_{ms}}{\bar{E}_{mn}} \left\{ s(s+1) b_{ms}^{(2)} \frac{h_s(x_0)}{x_0} - \sum_{l=1}^{\infty} a_l^{(2)} \right. \\
&\times \left[s(s+1) d_{msl} \frac{j_s(x_l)}{x_l} + \frac{\bar{w}_{msl}}{\lambda_l} j'_s(x_l) \right] \left. \right\} \frac{I_{7,msn}}{n(n+1)I_{mnn}} \\
&+ \sum_{s=n,n\pm 2,n\pm 4} \frac{\bar{E}_{ms}}{\bar{E}_{mn}} \left\{ s(s+1) p_{ms} \left[\Gamma_{1,s}^{(2)}(x_0) - \frac{j_s(x_0)}{x_0} \right] \right. \\
&+ s(s+1) b_{ms}^{(0)} \left[\Gamma_{3,s}^{(2)}(x_0) - \frac{h_s(x_0)}{x_0} \right] - \sum_{l=1}^{\infty} a_l^{(0)} s(s+1) d_{msl} \\
&\times \left[\Gamma_{1,s}^{(2)}(x_l) - \frac{j_s(x_l)}{x_l} \right] - \left. \sum_{l=1}^{\infty} a_l^{(0)} \frac{\bar{w}_{msl}}{\lambda_l} \left[E_{1,s}^{(2)}(x_l) - j'_s(x_l) \right] \right\} \\
&\times I_{8,msn} / [n(n+1)I_{mnn}], \tag{A.4}
\end{aligned}$$

where $E_{1,n}^{(2)}(x) = -xj''_n(x)/2$, $B_{1,n}^{(4)}(x) = 3xj'_n(x)/8 + x^2j''_n(x)/8$, $\Gamma_{1,n}^{(4)}(x) = -j_n(x)/(8x) + j'_n(x)/8 + xj''_n(x)/8$, $\Delta_{1,n}^{(4)}(x) = xj''_n(x)/2 + x^2j'''_n(x)/8 - j_n(x)/(8x) + j'_n(x)/8$, and for $B_{3,n}^{(4)}$, $\Gamma_{3,n}^{(4)}$, $\Delta_{3,n}^{(4)}$, we replace j_n, j'_n, j''_n, j'''_n with h_n, h'_n, h''_n, h'''_n , respectively. Finally,

$$\begin{aligned}
N_{1,msn} &= m^2 I_{msn} + I_{2,msn}, \\
N_{2,msn} &= -im [(s+n+2)I_{5,msn} - (s-m+1)I_{m,s+1,n} \\
&- (n-m+1)I_{m,s,n+1}], \\
N_{3,msn} &= m^2 I_{3,msn} + I_{4,msn}, \\
N_{4,msn} &= im [(s+n+2)I_{6,msn} - (s-m+1)I_{3,m,s+1,n} \\
&- (n-m+1)I_{3,m,s,n+1}]. \tag{A.5}
\end{aligned}$$

In all formulas herein, I_{msn} and $I_{k,msn}$, $k = 2, \dots, 8$ are integrals involving the associated Legendre functions and

their derivatives. Their analytical expressions are given in Appendix A of [33], where I_{msn} is denoted as $I(s, n)$, and $I_{k,msn}$ as $I_k(s, n)$. The expressions for $Y_{3,mn}^{(2)}$, $Y_{4,mn}^{(2)}$, $Y_{3,mn}^{(4)}$, $Y_{4,mn}^{(4)}$, are derived from those for $Y_{1,mn}^{(2)}$, $Y_{2,mn}^{(2)}$, $Y_{1,mn}^{(4)}$, $Y_{2,mn}^{(4)}$, respectively, by making the substitutions $q_{mn} \leftrightarrow p_{mn}$, $a_{mn} \leftrightarrow b_{mn}$, $c_{mnl} \rightarrow \tau_l d_{mnl}$, $d_{mnl} \rightarrow \tau_l c_{mnl}$, and setting $\bar{w}_{mnl} \equiv 0$.

REFERENCES

- [1] X. Lu, J. Han, and W. Zhang, "Localized plasmonic properties of sub-wavelength geometries resonating at terahertz frequencies," *IEEE J. Sel. Topic Quantum Electron.*, vol. 17, no. 1, pp. 119–129, Jan./Feb. 2011.
- [2] O. Y. Yermakov, A. A. Bogdanov, and A. V. Lavrinenko, "Broadband polarization degeneracy of guided waves in subwavelength structured ZnO pattern," *IEEE J. Sel. Topic Quantum Electron.*, vol. 25, no. 3, May/Jun. 2019, Art. no. 8200307, doi: 10.1109/JSTQE.2018.2886306.
- [3] W. Liu and Y. S. Kivshar, "Generalized Kerker effects in nanophotonics and meta-optics [Invited]," *Opt. Express*, vol. 26, pp. 13 085–13 105, 2018.
- [4] J. M. Geffrin *et al.*, "Magnetic and electric coherence in forward- and back-scattered electromagnetic waves by a single dielectric subwavelength sphere," *Nature Commun.*, vol. 3, 2012, Art. no. 1171.
- [5] Y. H. Fu, A. I. Kuznetsov, A. E. Miroschnichenko, Y. F. Yu, and B. Luk'yanchuk, "Directional visible light scattering by silicon nanoparticles," *Nature Commun.*, vol. 4, 2013, Art. no. 2538.
- [6] R. Gómez-Medina *et al.*, "Electric and magnetic dipolar response of germanium nanospheres: Interference effects, scattering anisotropy, and optical forces," *J. Nanophoton.*, vol. 5, 2011, Art. no. 053512.
- [7] K. Ullah *et al.*, "Light scattering by subwavelength Cu₂O particles," *Nanotechnology*, vol. 28, 2016, Art. no. 134002.
- [8] D. C. Tzarouchis, P. Ylä-Oijala, and A. Sihvola, "Resonant scattering characteristics of homogeneous dielectric sphere," *IEEE Trans. Antennas Propag.*, vol. 65, no. 6, pp. 3184–3191, Jun. 2017.
- [9] W. Liu, A. E. Miroschnichenko, D. N. Neshev, and Y. S. Kivshar, "Broadband unidirectional scattering by magneto-electric core-shell nanoparticles," *ACS Nano*, vol. 6, pp. 5489–5497, 2012.
- [10] Y. Li *et al.*, "Broadband zero-backward and near-zero-forward scattering by metallo-dielectric core-shell nanoparticles," *Sci. Rep.*, vol. 5, 2015, Art. no. 12491.
- [11] W. Liu, B. Lei, J. Shi, and H. Hu, "Unidirectional superscattering by multilayered cavities of effective radial anisotropy," *Sci. Rep.*, vol. 6, 2016, Art. no. 34775.
- [12] A. I. Kuznetsov, A. E. Miroschnichenko, M. L. Brongersma, Y. S. Kivshar, and B. Luk'yanchuk, "Optically resonant dielectric nanostructures," *Science*, vol. 354, no. 6314, pp. aag2472-1–aag2472-8, 2016.
- [13] I. Staude *et al.*, "Tailoring directional scattering through magnetic and electric resonances in subwavelength silicon nanodisks," *ACS Nano*, vol. 7, pp. 7824–7832, 2013.
- [14] X. Zambrana-Puyalto and N. Bonod, "Tailoring the chirality of light emission with spherical Si-based antennas," *Nanoscale*, vol. 8, pp. 10 441–10 452, 2016.
- [15] S. D. Campbell and R. W. Ziolkowski, "Near-field directive beams from passive and active asymmetric optical nanoantennas," *IEEE J. Sel. Topic Quantum Electron.*, vol. 21, no. 4, Jul./Aug. 2015, Art. no. 4800112.
- [16] D. A. Powell, M. Lapine, M. V. Gorkunov, I. V. Shadrivov, and Y. S. Kivshar, "Metamaterial tuning by manipulation of near-field interaction," *Phys. Rev. B*, vol. 82, 2010, Art. no. 155128.
- [17] A. E. Miroschnichenko, B. Luk'yanchuk, S. A. Maier, and Y. S. Kivshar, "Optically induced interaction of magnetic moments in hybrid metamaterials," *ACS Nano*, vol. 6, pp. 837–842, 2012.
- [18] B. S. Luk'yanchuk, N. V. Voshchinnikov, R. Paniagua-Domínguez, and A. I. Kuznetsov, "Optimum forward light scattering by spherical and spheroidal dielectric nanoparticles with high refractive index," *ACS Photon.*, vol. 2, pp. 993–999, 2015.
- [19] G. P. Zouros, A. D. Kotsis, and J. A. Roumeliotis, "Electromagnetic scattering from a metallic prolate or oblate spheroid using asymptotic expansions on spheroidal eigenvectors," *IEEE Trans. Antennas Propag.*, vol. 62, no. 2, pp. 839–851, Feb. 2014.
- [20] G. P. Zouros, A. D. Kotsis, and J. A. Roumeliotis, "Efficient calculation of the electromagnetic scattering by lossless or lossy, prolate or oblate dielectric spheroids," *IEEE Trans. Microw. Theory Techn.*, vol. 63, no. 3, pp. 864–876, Mar. 2015.
- [21] S. Asano and G. Yamamoto, "Light scattering by a spheroidal particle," *App. Opt.*, vol. 14, pp. 29–49, 1975.
- [22] M. F. R. Cooray and I. R. Ciric, "Scattering of electromagnetic waves by a coated dielectric spheroid," *J. Electromagn. Waves Appl.*, vol. 6, pp. 1491–1507, 1992.
- [23] W. J. Tropf, M. E. Thomas, and T. J. Harris, "Properties of crystals and glasses," in *Handbook of Optics*, vol. 2, M. Bass, Ed. New York, NY, USA: McGraw-Hill, 1995, ch. 33.
- [24] S. N. Papadakis, N. K. Uzunoglu, and C. N. Capsalis, "Scattering of a plane wave by a general anisotropic dielectric ellipsoid," *J. Opt. Soc. Am. A*, vol. 7, pp. 991–997, 1990.
- [25] S. Liu, L. W. Li, M. S. Leong, and T. S. Yeo, "Scattering by an arbitrarily shaped rotationally uniaxial anisotropic object: Electromagnetic fields and dyadic Green's functions," *J. Electromagn. Waves Appl.*, vol. 14, pp. 87–106, 2000.
- [26] A. Doicu, T. Wriedt, and Y. A. Eremin, *Light Scattering by Systems of Particles: Null-Field Method With Discrete Sources: Theory and Programs*. Berlin, Germany: Springer, 2006.
- [27] C. Flammer, *Spheroidal Wave Functions*. Stanford, CA, USA: Stanford Univ. Press, 1957.
- [28] Z. F. Lin and C. T. Chui, "Electromagnetic scattering by optically anisotropic magnetic particle," *Phys. Rev. E*, vol. 69, 2004, Art. no. 056614.
- [29] M. A. Yurkin and A. G. Hoekstra, "The discrete-dipole-approximation code ADDA: Capabilities and known limitations," *J. Quantitative Spectrosc. Radiative Transfer*, vol. 112, pp. 2234–2247, 2011.
- [30] J. L.-W. Li and W.-L. Ong, "A new solution for characterizing electromagnetic scattering by a gyroelectric sphere," *IEEE Trans. Antennas Propag.*, vol. 59, no. 9, pp. 3370–3378, Sep. 2011.
- [31] J. A. Stratton, *Electromagnetic Theory*. New York, NY, USA: McGraw-Hill, 1941.
- [32] P. M. Morse and H. Feshbach, *Methods of Theoretical Physics*. New York, NY, USA: McGraw-Hill, 1953.
- [33] A. D. Kotsis and J. A. Roumeliotis, "Electromagnetic scattering by a metallic spheroid using shape perturbation method," *Prog. Electromagn. Res.*, vol. 67, pp. 113–134, 2007.
- [34] B. García-Cámara, F. Moreno, F. González, J. M. Saiz, and G. Videen, "Light scattering resonances in small particles with electric and magnetic properties," *J. Opt. Soc. Am. A*, vol. 25, pp. 327–334, 2008.
- [35] M. Kerker, D.-S. Wang, and C. L. Giles, "Electromagnetic scattering by magnetic spheres," *J. Opt. Soc. Am.*, vol. 73, pp. 765–767, 1983.



Georgios D. Kolezas (S'17) was born in Athens, Greece, in 1977. He received the Electrical and Computer Engineering and Master of Science degrees from the National Technical University of Athens (NTUA), Athens, Greece, in 2002 and 2009, respectively, where he is currently working toward the Dr. Eng. degree.

Since 2014, he has been a Teaching Assistant with the School of Electrical and Computer Engineering, NTUA. His research interests include scattering and wave propagation in electromagnetic theory.



Grigorios P. Zouros (S'12–M'13–SM'17) was born in Lefkada, Greece, in 1982. He received the Electrical and Computer Engineering degree and the Dr. Eng. degree from the National Technical University of Athens (NTUA), Athens, Greece, in 2008 and 2012, respectively.

From 2008 to 2012, he was a Teaching Assistant with the School of Electrical and Computer Engineering, NTUA. From 2009 to 2013, he was a Laboratory Instructor with the Laboratory of Automatic Control Systems, School of Educational and Technological Engineering of Athens (ASPATE), Athens. From 2010 to 2011, he was a Visiting Researcher with the Delft Institute of Applied Mathematics, Delft University of Technology, Delft, The Netherlands. From 2013 to 2014, he fulfilled his military service at the Corps of Research and Computer Science. Since 2012, he has been a Postdoctoral Researcher with the School of Electrical and Computer Engineering, NTUA. Since 2015, he has been a Laboratory Instructor with the Laboratory of Power Electronics, ASPATE. His current research interests include the propagation and scattering of electromagnetic waves in elliptical, spheroidal, and anisotropic configurations, microwave cavities, and fast solvers for the electromagnetic scattering by inhomogeneous anisotropic 3-D objects.

Dr. Zouros served as an Expert of the Romanian UEFISCDI Executive Agency in 2011. He was the recipient of the Young Scientist Award of the International Conference on Mathematical Methods in Electromagnetic Theory (MMET) in 2010, the IEEE Student Paper Contest Award of the IEEE Applied Electromagnetics Conference and the IEEE Indian Antenna Week in 2011, and a candidate for the 2016 R. W. P. King Award of the IEEE TRANSACTIONS ON ANTENNAS AND PROPAGATION. He was a Session Chair of the IEEE MTT-S international conference NEMO 2017. He was awarded a Postgraduate Fellowship of Excellence (Siemens program) from the Greek State Scholarships Foundation (IKY) in 2017. He was a TPC member of the IEEE international conference MMET in 2018.



Kosmas L. Tsakmakidis was born in Komotini, Greece, in 1979. He received the Electrical and Computer Engineering diploma from the Aristotle University of Thessaloniki, Thessaloniki, Greece, in 2002, and the M.Res. (Master of Research) degree in electronic engineering and the Ph.D. degree in applied physics, both from the University of Surrey, Guildford, U.K., in 2003 and 2009, respectively.

From 2008 to 2013, he was a Royal Academy of Engineering Research Fellow, first with the University of Surrey and then (from 2011) with Imperial College London, London, U.K. From 2014 to 2015, he was a Postdoctoral Scholar with the Department of Mechanical Engineering, University of California, Berkeley, USA, and from 2015 to 2016, he was a Eugen Lommel Postdoctoral Fellow with the Max Planck—University of Ottawa Center for Extreme and Quantum Photonics and the Department of Physics, University of Ottawa, Canada. From 2017 to 2018, he was an EPFL Fellow with the Ecole Polytechnique Federale de Lausanne, Lausanne, Switzerland, and since March 2018, he has been an Assistant Professor with the Solid State Physics Section, Department of Physics, National and Kapodistrian University of Athens, Athens, Greece. He has introduced key concepts and results in the fields of metamaterials, nanophotonics, and slow light, and his work has been extensively covered by national and international news media, outlets, and popular magazines. His current research interests are in theoretical and computational condensed matter photonics, including nanophotonics, metamaterials, plasmonics, slow light, quantum and nonlinear optics, nonequilibrium physics, complexity science, and computational electrodynamics.

Dr. Tsakmakidis was an Associate Editor for the journal *Nature Materials* between 2012 to 2013. He was the recipient of the Institute of Physics Quantum Electronics and Photonics Ph.D. Thesis Prize in 2010, the Runner-up Prize in the Science, Engineering and Technology for Britain competition for early-stage researchers in 2010, bestowed by the Parliamentary and Scientific Committee of the House of Commons (England), the Researcher of the Year Award of the Faculty of Engineering and Physical Sciences, University of Surrey, in 2010, the Innovision Prize for Best Project by a student graduating with an MRes by the University of Surrey and Innovision Research and Technology in 2004, and the Third Prize by the Greek Mathematical Society (EME), among all Lyceum students on national level, Athens, in 1996.